Supplementary Material

Carbon nanotubes derived from waste cooking oil for the removal of emerging contaminants

Michelle Pains Duarte [a,1]; Rayane Cristian Ferreira Silva [a]; Tayline P. Viana de Medeiros [b,c]; José Domingos Ardisson [d]; Alexandre Alberto Chaves Cotta [e]; Rafik Naccache [b,c]; Ana Paula de Carvalho Teixeira [a*]

[a] Departamento de Química, ICEx, Universidade Federal de Minas Gerais, UFMG, Belo Horizonte, MG 31270-901

[b] Department of Chemistry and Biochemistry and the Centre for NanoScience Research, Concordia University, Montreal, QC, Canada, H4B 1R6

[c] Quebec Centre for Advanced Materials, Concordia University, Montreal, QC, Canada, H4B 1R6

[d] Centro de Desenvolvimento em Tecnologia Nuclear, CDTN, Belo Horizonte, MG 31270-901, Brazil.

[e] Departamento de Física, Universidade Federal de Lavras, UFLA, Lavras, MG 37200-000.

*anapct@ufmg.br

1 Materials and Methods

1.1 Characterization

Transmission Electron Microscopy (TEM)

The CNTs were dispersed in isopropanol and pipetted on carbon films (Holey Carbon – 300 mesh), supported on copper grids. TEM images were acquired using a Tecnai G2-20 – SuperTwin FEI microscope operating under 200 kV field emission.

Scanning Electron Microscopy (SEM)

The catalyst and CNTs were prepared on double-sided carbon tape and fixed in an aluminum sample holder. SEM images were acquired using a FEG – Quanta 3D FEI microscope, operated at a voltage of 5.0 kV under a high vacuum.

X-ray Diffraction (XRD)

The XRD analyses for the catalysts and CNTs were carried out on dried powder samples using a 2nd Gen D2 Phaser X-ray diffractometer (Bruker AXS). Diffraction patterns were acquired using a Cu Kα source at a 30 kV and 10 mA generator power, coupled with 2θ/θ scans in the continuous PSD fast scan mode. The scan range was set from 5 to 80º with a step size of 0.003º, an integration time of 2 s, and a position-sensitive detector opening of 4.7970º.

[1]Present addresses:
Department of Chemistry and Biochemistry and the Centre for NanoScience Research, Concordia University, Montreal, QC, Canada, H4B 1R6
Quebec Centre for Advanced Materials, Concordia University, Montreal, QC, Canada, H4B 1R6

Mössbauer Spectroscopy

The Mössbauer spectra of the catalyst and CNTs were collected at room temperature using a ^{57}Co source in an Rh matrix and α-Fe as a reference, with a conventional spectrometer operating in constant acceleration mode.

Nitrogen sorption analysis

The sorption/desorption isotherms of N_2, at 77 K, were obtained using Autosorb iQ equipment (Quantachrome Instruments, USA). 500 mg of the catalyst and 500 mg of each CNTs were degassed before the analysis at 200 °C for 6 h. The surface area was calculated using the BET method, while the pore size distribution was determined by the BJH method [1].

Thermogravimetric Analysis

Thermogravimetric analyses were performed on a DTG-60H analyzer from Shimadzu. CNTs samples were heated from 25 °C to 900 °C at a rate of 10 °C min^{-1} under an oxidizing atmosphere with a flow of 50 mL min^{-1}.

Raman Spectroscopy

Raman Spectroscopy analyses were carried out on Witec Alpha 300 spectrometer with an EMCCD detector, coupled with an atomic force microscope (AFM), belonging to the Nanomaterial Characterization and Processing Laboratory (LCPnano) from the Physics Department of Universidade Federal de Minas Gerais. The excitation wavelength of the laser used was 633 nm and a power of 1 mW. For materials synthesized from waste cooking oil, measurements were performed with 6 accumulations of 30 seconds, while for materials synthesized from ethyl acetate, measurements were performed with 3 accumulations of 60 seconds, at 3 different points of each sample. The spectra were obtained from the average of these points.

X-ray Photoelectron Spectroscopy (XPS)

The survey and high-resolution spectra of the CNTs were acquired using a Thermo Scientific K-alpha x-ray photoelectron spectrometer. Each analysis was performed at two different points in the sample, with 3 scans for each search spectrum and for the high resolution C 1s spectra and 10 scans for the high resolution O1s spectra. The averages were plotted for both the survey and high-resolution scans.

Point of zero charge (PZC)

The points of zero charge of the CNTs were determined by adding 30.0 mL of 0.1 M NaCl solution to several falcon tubes. The pH of the solution was adjusted between 2 and 12 by adding either 0.1 M of HCl and NaOH. Subsequently, 10 mg of each carbon material were added to the tubes. The tubes were shaken at 300 rpm (DSR-10B - Global Trade Technology) at 21 °C for 48 h. The suspensions were then filtered and, the final pH values of the solutions were determined. The pH_{PZC} was determined by plotting a graph of ΔpH (pH_{final}-pHi_{nitial}) versus pHi_{nitial}.

1.2 Adsorption studies

Kinetic study

The kinetic study was carried out under the same conditions as the contact test at different time intervals, in triplicate. The amount of each contaminant adsorbed at each interval of time (q_t) was determined using Eq.1:

$$q_t = \frac{(C_0 - C_e) * V}{m} \quad (1)$$

where q_t is the adsorption capacity at a certain time (mg g^{-1}), C_0 is the initial concentration (mg L^{-1}), C_e is the equilibrium concentration (mg L^{-1}), V is the solution volume (L) and m is the mass (g) of adsorbent. The data obtained were fitted to the pseudo-first-order and the pseudo-second-order models [2,3].

Adsorption isotherm study

The adsorption isotherm study was performed under the same conditions as prior tests. The solution concentrations used for the 17α-ethinylestradiol (EE2) were 1, 2, 5, 10, 20, 40, 60, 80 and 100 mg L^{-1}, while for the norfloxacin (NOR) were 2, 8, 10, 12, 15, 25, 30, 50 and 70 mg L^{-1}. The amount of each contaminant adsorbed in the equilibrium (q_e) was calculated using Eq.1.

The data obtained were fitted to the Langmuir and Freundlich models [3,4].

Non-linear chi-square analysis

The non-linear chi-square test, χ^2, Eq. 2, was performed in order to compare the experimental with the theoretical values. A small value of χ^2 indicates a small dispersion between theoretical and experimental values, while larger values indicate a greater dispersion between theoretical and experimental data.

$$\chi^2 = \sum \frac{(q_{exp} - q_{calc})^2}{q_{calc}} \tag{2}$$

2 Catalyst characterization

2.1 Scanning Electron Microscopy (SEM)

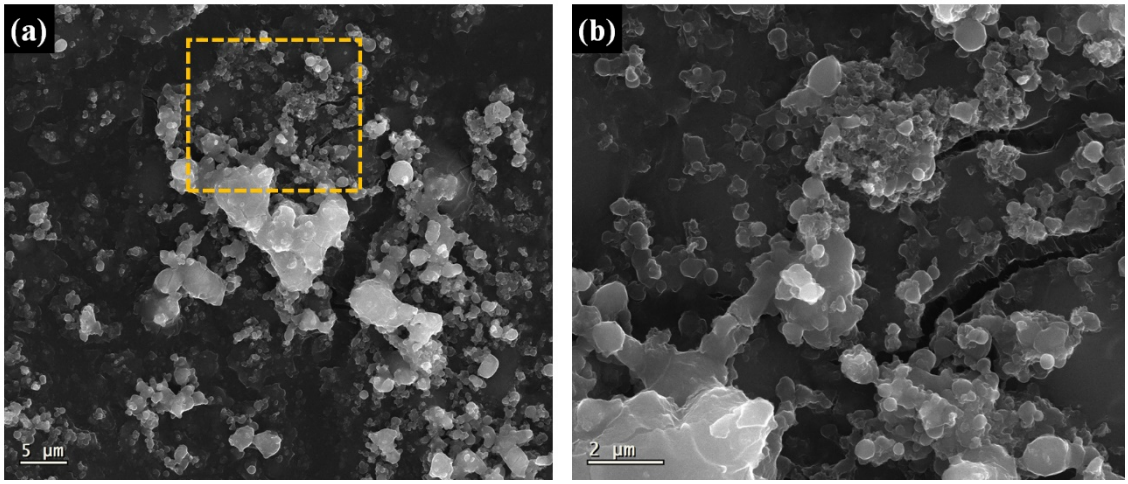

Figure S.1. Scanning electron micrographs of Fe-Mo/MgO catalyst: (a) general image; (b) enlargement of the yellow region in figure (a). It is possible to notice from the images that the catalyst has a heterogeneous morphology comprising agglomerates of particles of variable sizes and diameters. It is known that the diameter of the catalyst particles directly influences the diameter of the tubes to be synthesized [5,6]. Therefore, it is expected that the synthesized CNTs have different diameters.

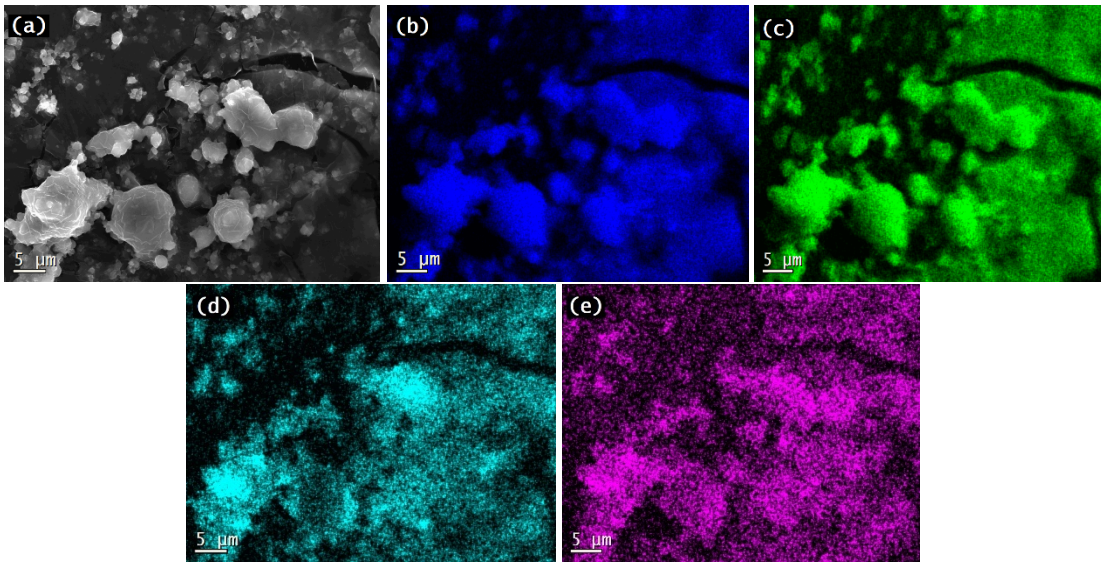

Figure S.2. EDS mapping images. (a) general image, (b) magnesium atoms are indicated in dark blue, (c) oxygen in green, (d) iron in teal, and (e) molybdenum in purple. It is possible to verify the uniform distribution of the elements via the surface of the material. As expected, it was possible to confirm the presence of MgO since the mapping indicates the presence of Mg and O accumulated at the same points. Furthermore, at these same points, it is possible to detect the presence of Fe and Mo, albeit less intense, due to the lower concentration of these elements compared to magnesium in the composition of the material.

2.2 X-ray Diffraction (XRD)

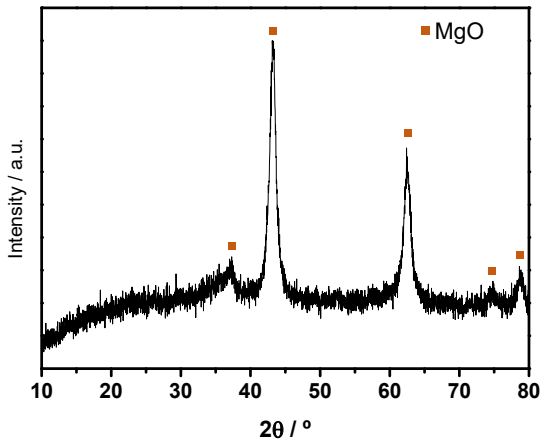

Figure S.3. X-ray diffractogram for the Fe-Mo/MgO catalyst. The catalyst diffractogram presents diffraction peaks at 37.33 °, 43.20 °, 62.45 °, 74.83 ° and 78.77 ° 2θ ascribed to magnesium oxide (JCPDS-45-946) [7]. Peaks related to the crystalline phases of the oxides of the metals Fe and Mo were expected, as these elements were identified through EDS analysis. However, none of these peaks were observed. The non-identification of peaks referring to these oxides may be related to the analysis procedure since the obtained diffractogram presented low intensity, in addition to noise. Hence, since the concentrations of Fe and Mo are low, lower intensity peaks were expected [8], which may have impaired its detection during the analysis and identification in the diffractogram due to the spectrum noise.

2.3 Mössbauer Spectroscopy

Table S.1. Hyperfine parameters for catalyst. It is possible to note the presence of Fe^{3+} ions in two different chemical environments since they present distinct values of isomeric shifts (δ) and quadrupole splittings (Δ). This result suggests the formation of different structures in the interaction of iron with the catalyst matrix. This result suggests the formation of different structures in the interaction of iron with the catalyst matrix, which may have contributed to the heterogeneous morphology of the catalyst pointed out in the SEM analysis

Sample	**Phases**	**δ (mm/s) ±(0.05 mm/s)**	**Δ/ε (mm/s) ±(0.05 mm/s)**	**B_{HF} (T) ±(0.5 T)**	**Relative area ±(1 %)**
FeMo/MgO	Fe^{3+}	0.30	0.57	-	71
	Fe^{3+}	0.27	1.07	-	29

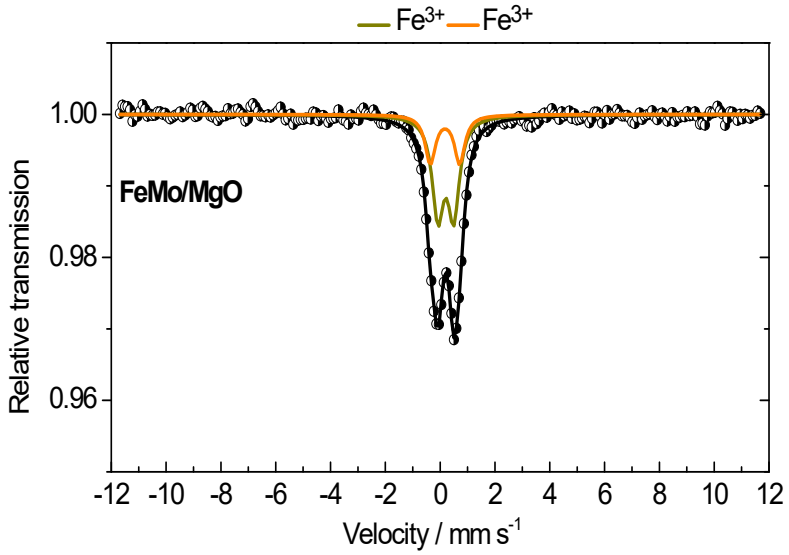

Figure S.4. Mössbauer spectrum for the Fe-Mo/MgO catalyst. It is possible to note the presence of two doublets, associated with Fe^{3+} ions, with isomeric shifts (δ) equal to 0.30 $mm.s^{-1}$ and 0.27 $mm.s^{-1}$ and quadrupole splittings (Δ) equal to 0.57 $mm.s^{-1}$ and 1.07 $mm.s^{-1}$, respectively. This fact indicates the presence of Fe^{3+} ions in different chemical environments [9]. The doublet with lower quadrupole splitting may be associated with superparamagnetic Fe^{3+} ions at the octahedral sites of the MgO crystal lattice, or possibly at the octahedral sites of the $MgFe_2O_4$ structure. The doublet with greater quadrupole splitting may be associated with cluster formation of octahedral Fe^{3+} ions with the MgO structure [10].

2.4 Nitrogen sorption analysis

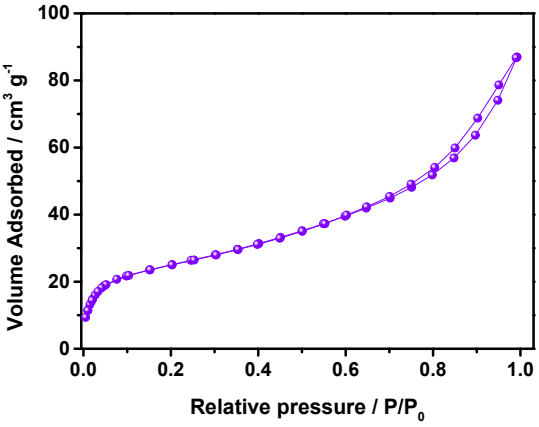

Figure S.5. Nitrogen sorption isotherm of Fe-Mo/MgO. The type II isotherm observed is associated with the adsorption of gases in non-porous or macroporous materials. In addition, it is possible to observe the presence of hysteresis, classified as type 3 (H3), which is generated by the existence of non-rigid or plate-type aggregates, indicating the presence of mesopores.[1] Aboul-Enein and Awadallah[11] obtained similar results and linked the presence of mixed oxides in the catalyst matrix, such as $MgFe_2O_4$ and $MgMoO_4$, with the creation of these mesopores. According to the authors, in the formation of these species, damage to the MgO matrix can occur, generating the mesopores. The surface area was calculated using the BET method (Brunauer-Emmet-Teller). The value found for the catalyst surface area was equal to 86.8 $m^2.g^{-1}$ The value obtained is within the values already reported in the literature [11,12].

3 Additional information on materials characterization

3.1 Mössbauer Spectroscopy

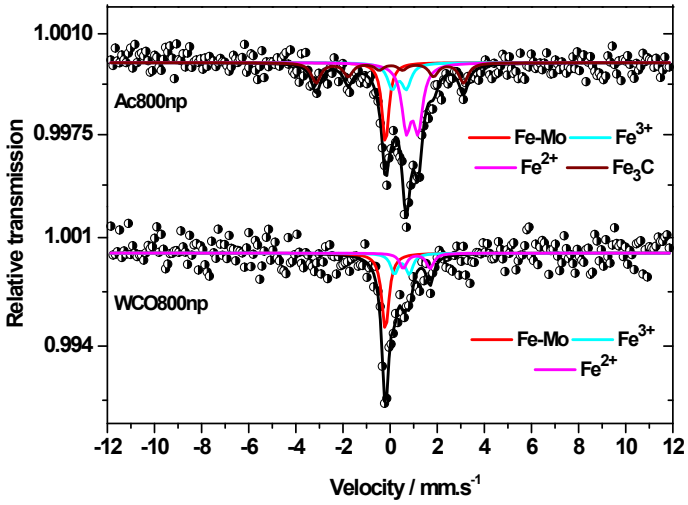

Figure S.6. Mössbauer spectra for unpurified Ac800 (Ac800np) and unpurified WCO800 (WCO800np). It was possible to observe the presence of a singlet with an isomeric shift equal to -0.09 in both spectra. This singlet is associated with the presence of the Fe-Mo alloy.[7] As the materials weren't purified, the catalyst matrix was still present on it. Thus, this result suggests the formation of the alloy between Fe and Mo during the reduction of the catalyst. Doublets assigned to Fe^{2+} ions and Fe^{3+} ions were also noticed in both spectra. Such phases can be associated with solid solutions of $(Mg_{1-x}Fe_x)O$ and $MgFe_2O_4$.[7,9,13] Furthermore, Ac800np presents a sextet with a magnetic field equal to 19.5 T and an isomeric shift equal to 0.18 mm s^{-1} associated with iron carbides, Fe_3C.[7]

Table S.2. Hyperfine parameters for Ac800np and WCO800np. It is possible to evidence the presence of the Fe-Mo alloy in both samples, suggesting its formation in the catalyst matrix. Phases related to Fe^{2+} ions $^{+}$ and Fe^{3+} ions were also noticed in both materials. In addition, Ac800np showed a phase related to iron carbides (Fe_3C).

Sample	Phases	δ (mm/s) ±(0.05 mm/s)	Δ/ε (mm/s) ±(0.05 mm/s)	B_{HF} (T) ±(0.5 T)	Relative area ±(1 %)
Ac800np	Fe-Mo	-0.09	-	-	15
	Fe^{2+}	1.04	0.50	-	42
	Fe^{3+}	0.48	0.60	-	16
	Fe_3C	0.18	0.04	19.5	27
WCO800np	Fe-Mo	-0.10	-	-	52
	Fe^{2+}	1.22	1.13	-	21
	Fe^{3+}	0.59	0.63	-	27

Table S.3. Hyperfine parameters for Ac800 and WCO800. It is possible to evidence the presence of three distinct phases of iron for each sample. For Ac800, phases related to Fe^{2+} ions, iron carbides (Fe_3C) and Fe-Mo alloy are seen while for WCO800 are seen phases related to austenite (γ-Fe(C)), Fe^{2+} and Fe^{3+} ions.

Sample	Phases	δ (mm/s) ±(0.05 mm/s)	Δ/ε (mm/s) ±(0.05 mm/s)	B_{HF} (T) ±(0.5 T)	Relative area ±(1 %)
Ac800	Fe-Mo	-0.09	-	-	43
	Fe^{2+}	1.04	0.56	-	15
	Fe_3C	0.18	0.04	19.5	42
WCO800	γ-Fe(C)	0.01	-	-	48
	Fe^{2+}	1.12	1.57	-	20
	Fe^{3+}	0.16	0.95	-	30

3.2 Thermogravimetric analysis of unpurified materials

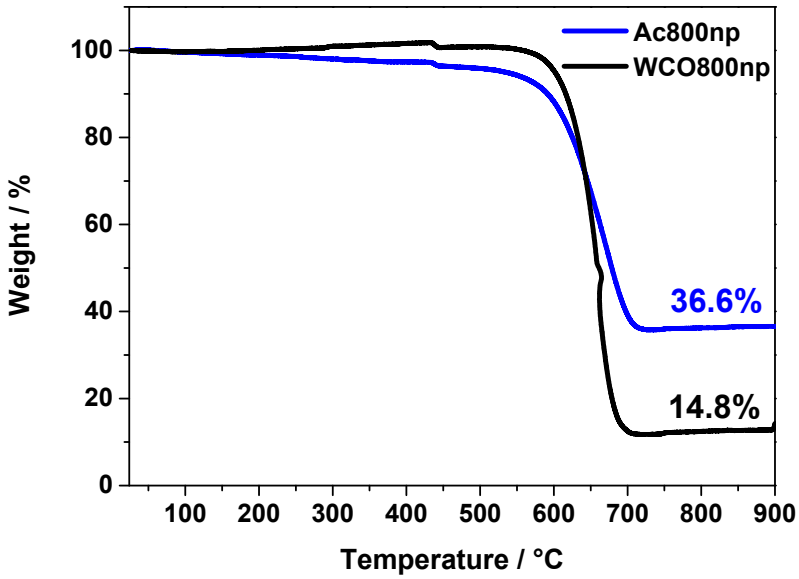

Figure S.7. TG curves for unpurified Ac800 (Ac800np) (blue) and unpurified WCO800 (WCO800np) (black). Residual masses, attributed to the oxides of the metals present in the catalyst used, equal to 36.6% and 14.8% are observed for Ac800np and WCO800np, respectively. It is estimated that the % carbon is 58.4% for Ac800np since an initial mass loss of ~5% and a residual mass of 36.6% are observed. In contrast, a value of 85.2% is noted for WCO800np since it presented a single step mass loss and a residual mass equal to 14.8%.

3.3 X-ray Photoelectron Spectroscopy (XPS)

Table S.4. XPS analysis results for Ac800 and WCO800. From the analysis of the broad spectra, it was found that both materials are made up mostly of carbon, with 98.9% and 99.2% for Ac800 and WCO800, respectively. Oxygen is present in low levels and may be associated with the carbon source used, the purification process, and surface contamination [14,15].

Sample	Element	Binding energy (eV)	Overall Percentage (atom%)
Ac800	C 1s	285.1	98.9
	O 1s	532.1	1.1
WCO800	C 1s	285.1	99.2
	O 1s	533.1	0.8

Table S.5. Deconvoluted high resolution XPS analysis results for Ac800 and WCO800. Both materials have similar compositions, having a higher percentage of C=C bonds (>90.0%). However, when analyzing the bonds between carbon and oxygen, it is observed that the material Ac800 presents a higher percentage of C=O bond while in the WCO800 material, the percentage of C-O/C-OH bonds is higher.

Sample	Element	Composition	Binding energy (eV)	Overall Percentage (atom%)
Ac800	C 1s	C=C	284.4	92.1
		C-OH / C-O-C	286.4	3.9
		C=O	288.0	4.0
		π-π	290.9	0.0
	O 1s	C=O	531.9	57.4
		C-O	533.1	42.6
WCO800	C 1s	C=C	284.4	91.0
		C-OH / C-O-C	286.2	5.7
		C=O	288.0	3.3
		π-π	290.8	0.0
	O 1s	C=O	531.0	27.3
		C-O	532.8	72.7

3.4 Nitrogen sorption analysis

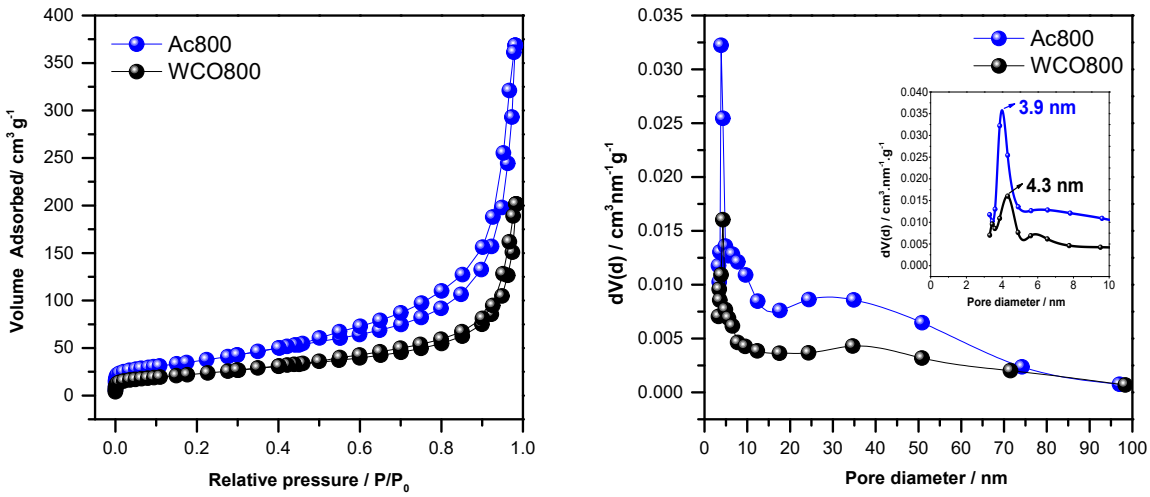

Figure S.8. **(a)** Nitrogen sorption isotherms and **(b)** pore distribution (BJH) diagram of Ac800 and WCO800. Both materials pointed to type II isotherms, which is characteristic of nonporous or microporous materials, and a small hysteresis, type H3, indicating the presence of mesoporous. Ac800 presented an average diameter pore equal to 3.9 and WCO800 equal to 4.3. This result is in agreement with the nitrogen sorption isotherms obtained since these pore sizes are typical of materials with mesoporous character.

Table S6. Adjustment results from the BET method for all materials. The specific surface areas of the materials Ac800 and WCO800 were determined using the BET method. It is observed that the material Ac800 had an area almost twice larger than the material WCO800. A parameter that deserves attention when applying the BET method is the constant C. This constant must always be positive for the information obtained to be considered reliable [1].

Sample	Surface Area / $m^2\ g^{-1}$	C constant
Ac800	128.4	139.3
WCO800	81.2	112.8

3.5 Point of zero charge (PZC)

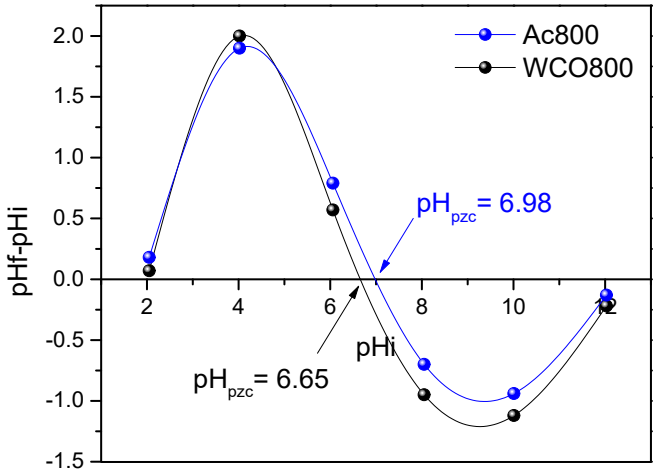

Figure S.9. Determination of pH_{PZC} of Ac800 and WCO800. It can be noticed through the ΔpH versus pHinitial curves, the pH_{PZC} value were 6.98 and 6.65 for Ac800 and WCO800, respectively. From the pH_{PZC} curve, it is possible to determine the surface charge of the material according to the pH of the solution. In solutions with pH values below pH_{PCZ}, the materials have a positively charged surface, being indicated for the adsorption of anionic compounds, while for solutions with pH values above pH_{PCZ} both materials have a negatively charged surface, being indicated for the adsorption of cationic compounds [16].

4 Additional information on adsorption studies

4.1 Calibration curves

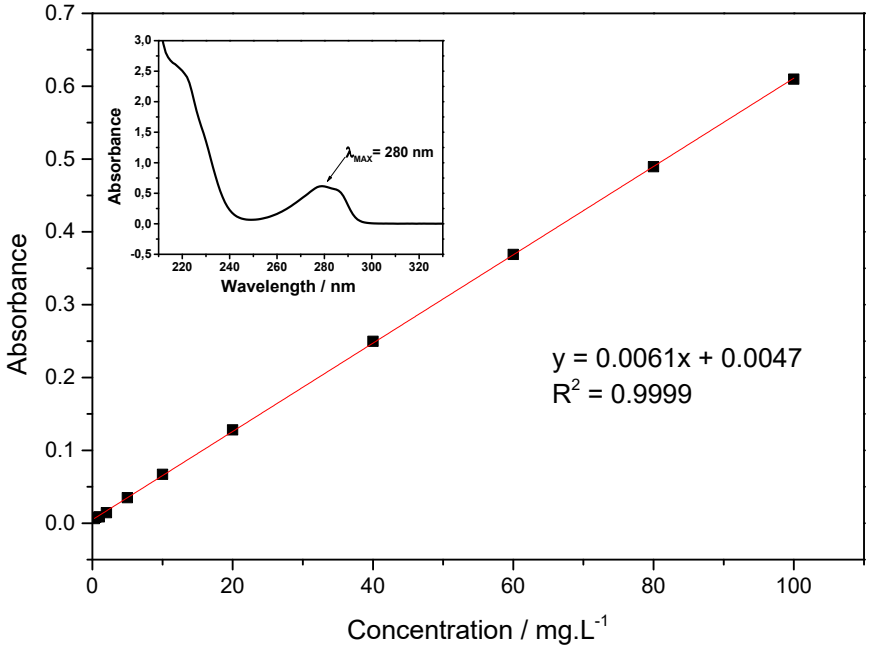

Figure S.10. Calibration curve for 17α-ethinylestradiol. The absorption spectrum of each concentration was measured in triplicate to ensure accuracy and the absorbance average of these points was used to obtain the curve. The calibration curve was obtained by varying the concentration of 17α-ethinylestradiol from 0.3 ppm to 100 $mg.L^{-1}$, at pH 7.6.

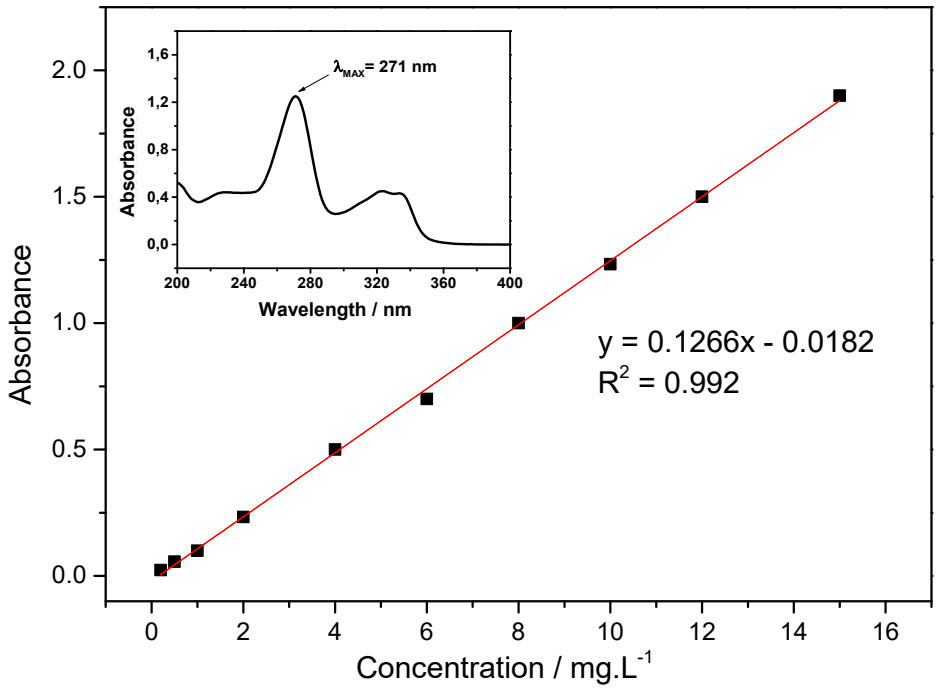

Figure S.11. Calibration curve for norfloxacin. The absorption spectrum of each concentration was measured in triplicate to ensure accuracy and the absorbance average of these points was used to obtain the curve. The calibration curve was obtained by varying the concentration of norfloxacin from 0.2 ppm to 15 $mg.L^{-1}$, at pH 7.6.

4.2 Results of kinetic and isotherm study models

Table S.7. Results of the adjustments of the kinetic models of pseudo-first order and pseudo-second order for EE2 and NOR on adsorption by Ac800 and WCO800, at pH = 7.6, 21 °C and concentration 10 mg L^{-1}. Through the data presented in the table, it is noted that the pseudo-second order kinetic model presented the highest correlation coefficients (R^2) and lowest chi-square values (χ^2). These results suggest that this model best describes for the four systems studied.

	Sample/Contaminant			
	Ac800/ EE2	**WCO800/ EE2**	**Ac800/ NOR**	**WCO800/ NOR**
Pseudo-first order	q_e= 8.8977	q_e= 7.2359	q_e= 8.0154	q_e= 7.3841
	k_1= 0.5416	k_1= 0.7218	k_1= 0.6773	k_1= 0.7195
	R^2= 0.9637	R^2= 0.9722	R^2= 0.9854	R^2= 0.9569
	χ^2= 0.3461	χ^2= 0.1611	χ^2= 0.0880	χ^2= 0.2783
Pseudo-second order	q_e= 9.5412	q_e= 7.7925	q_e= 8.7590	q_e= 7.8868
	k_2= 0.0809	k_2= 0.1232	k_2= 0.1030	k_2= 0.1208
	R^2= 0.9961	R^2= 0.9980	R^2= 0.9992	R^2= 0.9936
	χ^2= 0.0373	χ^2= 0.0918	χ^2= 0.0043	χ^2= 0.1148

q_e (mg g^{-1}): solute mass adsorbed per unit adsorbent mass at equilibrium; k_1 (min^{-1}): rate constant of first-order; k_2 (g mg^{-1} min^{-1}): rate constant of second-order;

Table S.8. Results of the adjustment of the Langmuir and Freundlich models for EE2 and NOR adsorption by Ac800 and WCO, at pH 7.6 and 21 ° C. Evaluating the data presented in the table, it is noted that for the contaminant 17α-ethinylestradiol, the model that best fit was the Freundlich model with highest correlation coefficients (R^2) and lowest chi-square values (χ^2) while for the contaminant norfloxacin, the model that best fit was the Langmuir model. This result suggests that adsorbate defined the type of adsorption that occurred, regardless of the material used.

	Sample/Contaminant			
	Ac800/EE2	**WCO800/EE2**	**Ac800/NOR**	**WCO800/NOR**
Langmuir	q_{max}= 50.6162	q_{max}= 28.3050	q_{max}= 44.7412	q_{max}= 23.9689
	K_L= 0.1560	K_L= 0.1751	K_L= 2.8880	K_L= 3.2787
	R^2= 0.9629	R^2= 0.9587	R^2= 0.9405	R^2= 0.9817
	χ^2= 14.1962	χ^2= 22.8202	χ^2= 2.2891	χ^2= 0.2697
Freundlich	K_F= 12.3799	K_F= 8.2334	K_F= 24.3529	K_F= 14.9902
	n= 2.8794	n= 3.4655	n= 3.8561	n= 6.2157
	R^2= 0.9844	R^2= 0.9855	R^2= 0.8997	R^2= 0.9169
	χ^2= 0.3204	χ^2= 5.1873	χ^2= 4.7893	χ^2= 2.4759

q_{max} (mg g^{-1}): maximum adsorption capacity; K_L (L mg^{-1}): constant of the Langmuir isotherm; K_F ($mg^{(1-1/n)}$ $L^{1/n}$ g^{-1}): constant of the Freundlich isotherm; n: constant related with the heterogeneity of the adsorbate sites;

Table S.9. Maximum adsorption capacities of Ac800 and WCO800. the maximum adsorption capacity of each material for each contaminant was estimated using the last point of each isotherm [17]. It is observed that the material Ac800p presented a greater adsorption capacity for both contaminants, which may be associated with its greater surface area.

Contaminant	**q_{max} Ac800 / mg g^{-1}**	**q_{max} WCO800 / mg g^{-1}**
17α-ethinylestradiol	48.91	26.94
Norfloxacin	46.21	24.45

References

1 M. Thommes, K. Kaneko, A. V. Neimark, J. P. Olivier, F. Rodriguez-Reinoso, J. Rouquerol and K. S. W. Sing, *Pure Appl. Chem.*, 2015, **87**, 1051–1069.

2 J. P. Simonin, *Chem. Eng. J.*, 2016, **300**, 254–263.

3 R. Ferreira do Nascimento, A. ; Clecius Alves De Lima, C. ; Bastos Vidal, D. ; de Quadros Melo and G. Santiago Cabral Raulino, *Adsorção: aspectos teóricos e aplicações ambientais*, 2014.

4 M. A. Al-Ghouti and D. A. Da'ana, *J. Hazard. Mater.*, 2020, **393**, 122383.

5 M. Kumar and Y. Ando, *J. Nanosci. Nanotechnol.*, 2010, **10**, 3739–3758.

6 J. P. Tessonnier and D. S. Su, *ChemSusChem*, 2011, **4**, 824–847.

7 A. P. C. Teixeira, B. R. S. Lemos, L. A. Magalhaes, J. D. Ardisson, R. M. Lago, C. A. Furtado and A. P. Santos, *J. Nanosci. Nanotechnol.*, 2012, **12**, 2661–2667.

8 A. E. Awadallah, A. A. Aboul-Enein, M. A. Azab and Y. K. Abdel-Monem, *Fullerenes Nanotub. Carbon Nanostructures*, 2017, **25**, 256–264.

9 V. Carles and A. Rousset, *Solid State Ionics*, 1996, **83**, 309–321.

10 P. Coquay, A. Peigney, E. De Grave, E. Flahaut, R. E. Vandenberghe and C. Laurent, *J. Phys. Chem. B*, 2005, **109**, 17813–17824.

11 A. A. Aboul-Enein and A. E. Awadallah, *Chem. Eng. J.*, 2018, **354**, 802–816.

12 B. Wang, X. Li, P. Chen and B. Zhu, *J. Alloys Compd.*, 2019, **786**, 440–448.

13 X. Ge, M. Li and J. Shen, *J. Solid State Chem.*, 2001, **161**, 38–44.

14 I. Pełech, R. Pełech, A. Kaczmarek, A. Jędrzejewska and D. Moszyński, *Int. J. Mater. Res.*, 2016, **107**, 35–43.

15 O. A. Gurova, V. E. Arhipov, V. O. Koroteev, T. Y. Guselnikova, I. P. Asanov, O. V. Sedelnikova and A. V. Okotrub, *Phys. Status Solidi Basic Res.*, 2019, **256**, 1–6.

16 F. M. Machado, C. P. Bergmann, E. C. Lima, M. A. Adebayo and S. B. Fagan, *Mater. Res.*, 2014, **17**, 153–160.

17 R. C. F. S. Silva, J. D. Ardisson, A. A. C. Cotta, M. H. Araujo and A. P. de C. Teixeira, *Environ. Pollut.*, 2020, **260**, 1–9.